Scripta Materialia 264 (2025) 116711

Contents lists available at ScienceDirect

Scripta Materialia

journal homepage: www.journals.elsevier.com/scripta-materialia

Improving hydrogen embrittlement resistance in high-strength martensitic steels via thermomechanical processing

Xiaodong Lan *, Kazuho Okada, Rintaro Ueji, Akinobu Shibata

Research Center for Structural Materials, National Institute for Materials Science, 1-2-1 Sengen, Tsukuba, Ibaraki 305-0047, Japan

ARTICLE INFO

Keywords:
Hydrogen embrittlement
Intergranular fracture
Martensitic steel
Dynamic ferrite transformation
Thermomechanical processing

ABSTRACT

This study proposes a novel approach for architecting dual-phase heterostructure to enhance hydrogen embrittlement resistance in high-strength martensitic steels while maintaining a tensile strength above 1200 MPa. Through thermomechanical processing, a unique dual-phase structure was achieved, characterized by a refined martensitic substructure and dynamically transformed ferrite grains along the prior austenite grain boundaries (PAGBs). Lowering the deformation temperature increased the ferrite volume fraction and the coverage of PAGBs by fine ferrite grains, which consequently reduced the area fraction of hydrogen-related intergranular fracture. Notably, 60 % compression at 700 °C completely suppressed hydrogen-related intergranular fracture, demonstrating an exceptional combination of strength and ductility even in hydrogen-charged state. The coverage of PAGBs by dynamically transformed ferrite was a critical factor in enhancing the hydrogen embrittlement resistance, with higher coverage correlating with improved hydrogen embrittlement resistance. These findings provide valuable microstructure design concepts for high-strength martensitic steels with superior hydrogen embrittlement resistance.

The global pursuit of carbon neutrality and the rising adoption of hydrogen-based technologies have significantly increased the demand for advanced high-strength steels. However, high-strength steels, particularly martensitic steels, are susceptible to hydrogen embrittlement [1,2]. Due to the increased susceptibility to hydrogen embrittlement with increasing strength level and the often-unavoidable hydrogen ingress during steel production or service, developing engineering solutions that enable both high hydrogen embrittlement resistance and excellent mechanical performance is crucial for the application of high-strength martensitic steels.

Intergranular and quasi-cleavage are typical fracture modes in hydrogen embrittlement. Generally, increasing hydrogen content shifts the fracture mode from quasi-cleavage to intergranular, leading to more severe brittleness [3,4]. Therefore, suppressing hydrogen-related intergranular fracture should be a priority for improving material reliability. As a typical microstructure of high-strength low- and medium-carbon steels, lath martensite comprises several structural units with different length scales: lath, block, packet, and prior austenite grain [5–7]. Despite the martensitic structures contain various types of high-angle boundaries, namely, block boundaries, packet boundaries, and prior austenite grain boundaries (PAGBs), hydrogen-related intergranular fracture mainly occurs on PAGBs [8–11]. This could be due to hydrogen accumulation around PAGBs during deformation [12,13] and has been discussed in terms of hydrogen-enhanced decohesion [14,15], hydrogen-enhanced localized plasticity [16–18], and hydrogen-enhanced strain-induced vacancy [19,20], etc. Recent studies highlight the potential of crystallographic tailoring at PAGBs and grain boundary engineering to mitigate hydrogen-related fractures. For instance, Archie et al. [21] and Shibata et al. [9,22,23] emphasized the importance of low-angle PAGB segments in preventing intergranular cracking, using micro-cantilever bending tests and multiscale three-dimensional analysis, respectively. In another approach, Okada et al. [24,25] demonstrated that carbon segregation at PAGBs can suppress the hydrogen-related intergranular fracture in martensitic steels, although this effect diminishes when diffusible hydrogen content exceeds 0.5 wt. ppm. Pinson et al. [26] reported that aluminum-induced ferritic microfilm along PAGBs can delay the hydrogen-related fractures in martensitic steels. However, the ferritic microfilm becomes embrittled and loses its ability to influence the crack propagation under slow deformation rates in hydrogen-rich environments.

Inspired by the aforementioned findings, this study proposes a microstructural design strategy to improve the resistance to hydrogen

* Corresponding author.
E-mail address: LAN.Xiaodong@nims.go.jp (X. Lan).

https://doi.org/10.1016/j.scriptamat.2025.116711
Received 30 January 2025; Received in revised form 12 April 2025; Accepted 14 April 2025
Available online 16 April 2025

embrittlement in high-strength martensitic steels via thermomechanical processing. This approach is based on the following mechanism: Dynamic ferrite transformation preferentially occurs along PAGBs during thermomechanical processing under specific conditions [27,28], and the resulting ferrite-martensite interfaces are more resistant to hydrogen than PAGBs [15,29]. This study aims to optimize the thermomechanical processing parameters and identify the critical microstructural factors that contribute to improved hydrogen embrittlement resistance in high-strength martensitic steels.

An Fe-3Mn-0.2C ternary alloy (Mn: 3.02, C: 0.18, Si: 0.01, P: < 0.002, S: 0.001, Al: 0.002, O: 0.001. N: 0.002, and Fe: balance (wt. %)) was used in the present study. The A_{e3} and A_{e1} temperatures calculated using Thermo-Calc software (database: TCFE7) are 762 °C and 622 °C, respectively. Cylindrical specimens, 24 mm in height and 16 mm in diameter, were machined from the as-received ingot by electrical discharge machining and then processed using a thermomechanical processing simulator (Fuji Electronic Industrial Co. Ltd.: Thermecmastor). The detailed thermomechanical processing steps are schematically illustrated in Fig. 1(a). The cylindrical specimens were first austenitized at 900 °C for 300 s, then cooled by nitrogen gas at a rate of 15 °C·s^{-1} to the deformation temperatures of 700~775 °C. After holding for 30 s to stabilize the temperature, each specimen was subjected to uniaxial compressive deformation with a 60 % reduction in height at a strain rate of 1 s^{-1}, followed by immediate unloading and nitrogen gas cooling to obtain hot compressed (HC) specimens. Specimens deformed at 775 °C, 750 °C, and 700 °C are designated as 775HC, 750HC, and 700HC, respectively. For comparison, as-quenched (AQ) martensite was prepared by direct quenching after the same austenitization treatment. Fig. 1(b) shows the apparent true stress–true strain curves of the specimens compressed at 775 °C, 750 °C, and 700 °C, assuming uniform deformation and constant volume. The steady-state flow stress indicates a balance between work hardening and dynamic softening during deformation.

The microstructures at the centers of sections parallel to the compression axis (CA) were characterized using optical microscopy (OM), backscattered electron (BSE) imaging, and electron backscattering diffraction (EBSD) in scanning electron microscope (SEM, Zeiss Sigma and Zeiss Crossbeam) equipped with a Bruker QUANTAX EBSD system. The pixel-counting method was used to measure the coverage of PAGBs by dynamically transformed ferrite grains in OM images. Micro-tensile specimens (gauge length: 3 mm, width: 1 mm, thickness: ~0.7 mm) were extracted from the centers of the compressed specimens, with the tensile loading direction (LD) set perpendicular to the CA. Zhao et al. [27] confirmed that the small-sized specimens could provide stress–-strain behaviors equivalent to standard-sized specimens made from an ultrafine-grained material. The micro-tensile specimens were mechanically and electrolytically polished, then cathodically pre-charged with hydrogen in an aqueous solution of 3 % NaCl and 3 $g{\cdot}L^{-1}$ NH_4SCN at a current density of 3 $A{\cdot}m^{-2}$ for 24 h at room temperature. Uniaxial tensile tests were conducted at an initial strain rate of 8.3×10^{-6} s^{-1} at room temperature in air. The fracture surfaces were observed by SEM after tensile testing. The diffusible hydrogen content (H_D) was measured by thermal desorption spectrometry (TDS) at a heating rate of 100 °C·h^{-1} using a R-DEC HTDS-004 system. The tensile tests and TDS measurements began 30 min after completing hydrogen pre-charging.

Fig. 2 shows (a_1, b_1, c_1, d_1) the OM images, (a_2, b_2, c_2, d_2) the image quality (IQ) + phase maps, and (a_3, b_3, c_3, d_3) the IQ + inverse pole figure (IPF) maps of the AQ (a_1–a_3), 775HC (b_1–b_3), 750HC (c_1–c_3), and 700HC (d_1–d_3) specimens. In the OM images, ferrite appeared as the lightly etched phase, with "F" and "M" denoting ferrite and martensite,

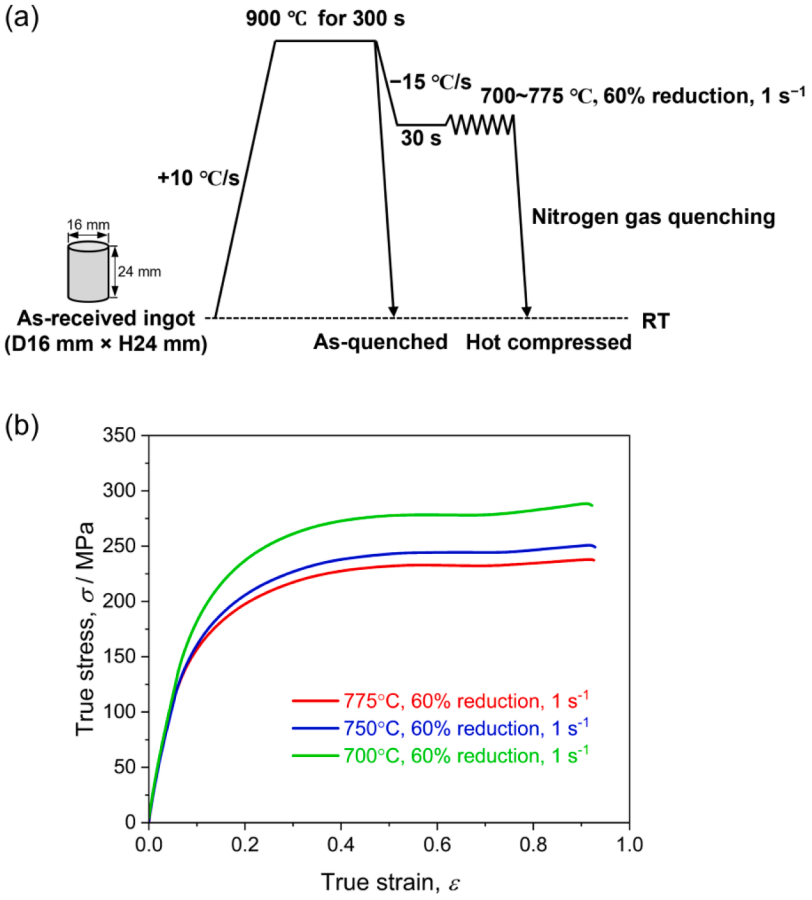

Fig. 1. (a) Schematic illustration of the thermomechanical processing steps; (b) Apparent true stress–true strain curves for the specimens compressed at 775 °C, 750 °C, and 700 °C.

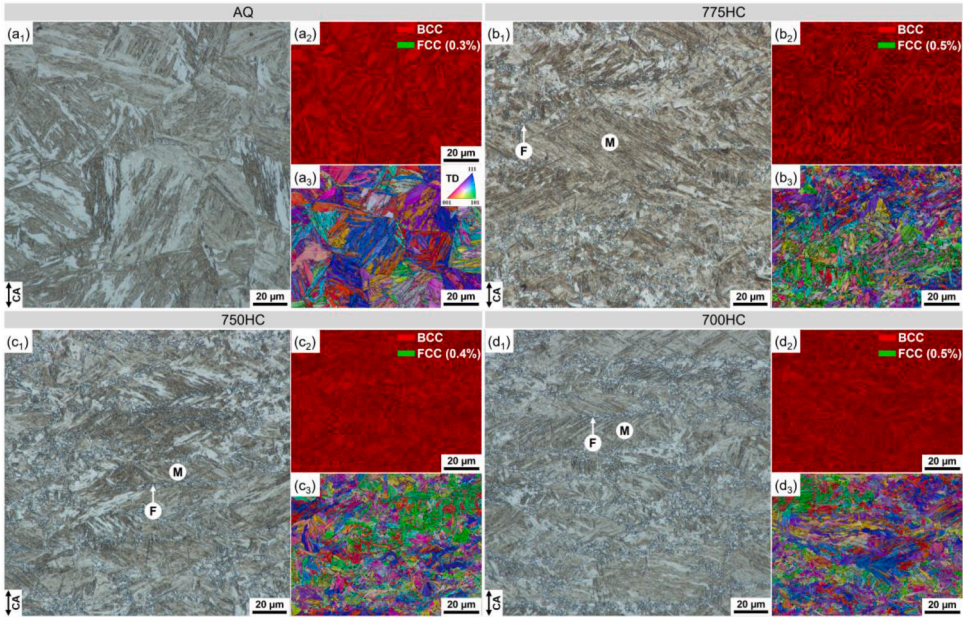

Fig. 2. (a_1, b_1, c_1, d_1) OM images, (a_2, b_2, c_2, d_2) IQ + phase maps, and (a_3, b_3, c_3, d_3) IQ + IPF maps of the AQ (a_1–a_3), 775HC (b_1–b_3), 750HC (c_1–c_3), and 700HC (d_1–d_3) specimens. The colors in the IPF map express the orientation parallel to the transverse direction (TD) of the specimen according to the stereographic triangle.

respectively. Hou et al. [30] reported that static ferrite transformation did not occur at temperatures above A_{e1} in Fe-3Mn-0.1C steel, even after extended holding for 100,000 s. Meanwhile, Shibata et al. [31] demonstrated that dynamic ferrite transformation occurred during the compression of Fe-2Mn-0.1C steel, as confirmed by *in-situ* neutron diffraction analysis. Therefore, the observed ferrite in the current specimens can be reasonably attributed to dynamic transformation. The phase maps confirmed that all specimens predominantly exhibited a body-centered cubic (BCC) structure, with less than 0.5 % of retained austenite in a face-centered cubic (FCC) structure. The OM and EBSD results showed that the AQ specimen exhibited a hierarchical martensitic microstructure consisting of blocks and packets within equiaxed prior austenite grains. In contrast, the HC specimens exhibited elongated prior austenite grains and dynamically transformed ferrite grains along the PAGBs. The average grain size of the dynamically transformed ferrite, measured using the line intercept method on BSE images (not shown), was approximately 0.85 μm. Moreover, the ferrite volume fractions were 4.2 %, 7.5 %, and 10.4 % for the 775HC, 750HC, and 700HC specimens, respectively, with corresponding PAGB coverages of 39 %, 63 %, and 87 %. Namely, both the volume fraction of ferrite and its coverage along the PAGBs increased as the deformation temperature decreased. Additionally, thermomechanical processing resulted in finer blocks and packets compared to those in the AQ specimen. This refinement aligns with the findings by Kawata et al. [32], and they proposed that the strengthening effect of austenite through ausforming resulted in the refinement of blocks with greater self-accommodation during transformation.

Fig. 3 shows the H_D in the hydrogen-charged AQ, 775HC, 750HC, and 700HC specimens, as measured by TDS. Despite the identical hydrogen-charging conditions, the specimens exhibited varying H_D values: 0.78 wt. ppm for the AQ specimen, 1.17 wt. ppm for the 775HC specimen, 1.22 wt. ppm for the 750HC specimen, and 1.38 wt. ppm for the 700HC specimen. The H_D in the AQ specimen was significantly lower than that in the HC specimens. Furthermore, the H_D slightly increased as the deformation temperature decreased. The increase in H_D with decreasing deformation temperature can be attributed to a higher density of hydrogen-trapping sites, such as variant boundaries and lattice defects, generated at lower deformation temperatures.

Fig. 4(a–d) present the nominal stress–nominal strain curves for the AQ, 775HC, 750HC, and 700HC specimens, respectively, with and

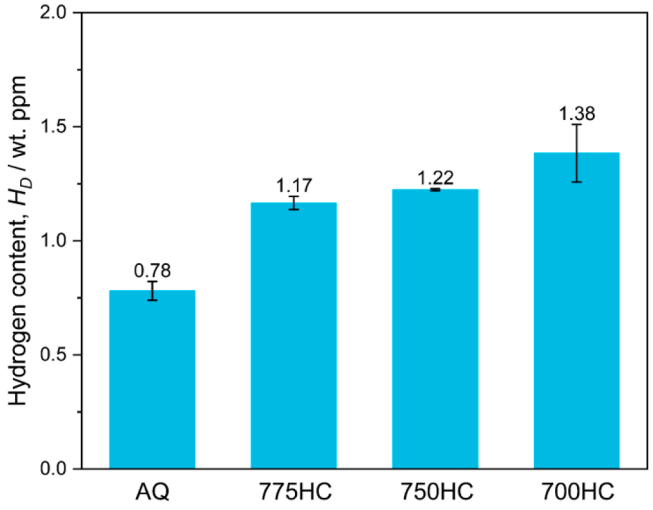

Fig. 3. Comparison of the H_D in the hydrogen-charged AQ, 775HC, 750HC, and 700HC specimens.

without hydrogen pre-charging. The strength level of the HC specimens remains consistently high, with tensile strength exceeding 1200 MPa for the uncharged specimens (blue curves), even when dynamically transformed ferrite formed via thermomechanical processing. This strength retention can be attributed to the high dislocation density (as evidenced by the kernel average misorientation maps in Supplemental Figure A1) in martensite, inherited from deformed austenite, along with the refined blocks, packets, and the fine-grained structure of dynamically transformed ferrite. The overall tensile strength of the HC specimens is governed by a competition between ferrite-induced softening and abovementioned strengthening mechanisms. The maximum tensile stress and total elongation for each condition are summarized in Fig. 4 (e) and (f), respectively. In the hydrogen-charged AQ specimen, the maximum tensile stress decreased moderately, while the total elongation dropped drastically compared to the uncharged counterpart. The hydrogen-charged 775HC specimen exhibited an even greater reduction in both stress-bearing capacity and total elongation. In contrast, the

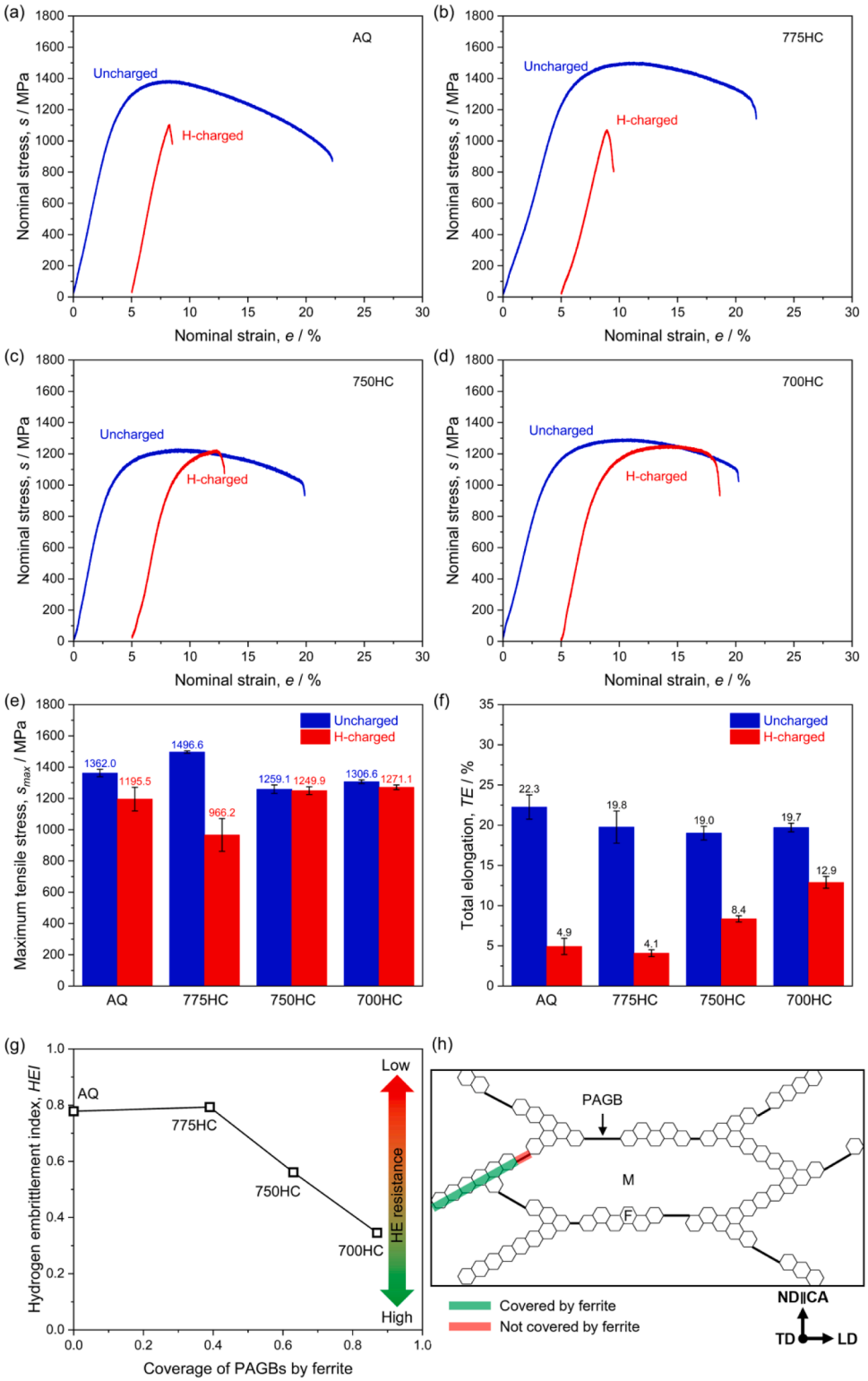

Fig. 4. (a–d) Nominal stress–nominal strain curves for the uncharged and hydrogen-charged specimens; (e) Maximum tensile stress comparison between specimens with and without hydrogen; (f) Total elongation comparison between specimens with and without hydrogen; (g) *HEI* as a function of PAGB coverage by ferrite grains; (h) Schematic of the microstructure after thermomechanical processing.

hydrogen-induced mechanical degradation was substantially suppressed in the 750HC and 700HC specimens. In particular, the hydrogen-charged 700HC specimen maintained a tensile strength exceeding 1200 MPa and an impressive total elongation of 12.9 %, despite having the highest H_D. To quantitatively evaluate the hydrogen embrittlement susceptibility, the hydrogen embrittlement index (*HEI*) was introduced. The *HEI* is defined as the fractional reduction in total elongation:

$$HEI = \frac{e_{TE} - e_{TE\_H}}{e_{TE}} \quad (1)$$

where e_{TE} and e_{TE_H} represent the total elongation of specimens without

and with hydrogen, respectively. A higher *HEI* indicates greater susceptibility to hydrogen embrittlement. Fig. 4(g) shows the relationship between the *HEI* and the coverage of PAGBs by ferrite, while Fig. 4(h) provides a schematic of the microstructure after thermomechanical processing, showing how this coverage was measured and the alignment of PAGB segments with respect to the LD. Obviously, the enhanced resistance to hydrogen embrittlement positively correlated with the increased PAGBs coverage by dynamically transformed ferrite.

Fig. 5 shows the SEM images of the fracture surfaces for the (a_1–d_1, a_2–d_2) uncharged and (e_1–h_1, e_2–h_2) hydrogen-charged specimens after tensile testing. The uncharged specimens predominantly exhibited ductile fracture, characterized by dimple patterns (Fig. 5(a_2–d_2)). In contrast, the hydrogen-charged specimens (Fig. 5(e_2–h_2)) showed characteristics of hydrogen-related fracture, displaying intergranular and quasi-cleavage fracture features. Specifically, the fracture surface of the hydrogen-charged AQ specimen was primarily intergranular, with a few quasi-cleavage regions. In comparison, the hydrogen-charged 775HC specimen showed a significantly lower fraction of intergranular fracture and smaller intergranular facets. The quasi-cleavage facets were also reduced in size due to the refinement of blocks and packets by thermomechanical processing. As the deformation temperature decreased, the area fraction of intergranular fracture further decreased, despite a slight increase in H_D (refer to Fig. 3). The hydrogen-charged 750HC specimen predominantly exhibited quasi-cleavage fracture with minor intergranular fracture (smaller facets), whereas the hydrogen-charged 700HC specimen displayed only quasi-cleavage fracture, indicating the complete suppression of hydrogen-related intergranular fracture.

Based on the results in Figs. 4 and 5, we conclude that the coverage of PAGBs by dynamically transformed ferrite plays a critical role in improving the hydrogen embrittlement resistance in high-strength martensitic steels. As the deformation temperature decreased, the volume fraction of ferrite and its coverage along the PAGBs increased, driven by accelerated dynamic ferrite transformation kinetics due to a higher density of defects at lower deformation temperatures [31,33]. This increase in PAGBs coverage correlated with a reduction in the area fraction of hydrogen-related intergranular fracture, as shown in Fig. 5. At 700 °C, the coverage reached a critical threshold, completely suppressing hydrogen-related intergranular fracture (Fig. 5(h_2)) and achieving an exceptional balance of strength and ductility in the hydrogen-charged state (Fig. 4(e–f)). The improved hydrogen embrittlement resistance can be attributed to several key factors. First, the formation of ferrite grains along the PAGBs reduced the area fraction of hydrogen-susceptible PAGB planes. When the PAGBs coverage is low, specific PAGB segments—particularly those with low cohesive energy and high local hydrogen concentration—can serve as potential sites for crack initiation and propagation. As the PAGBs coverage increased, the probability of hydrogen-related intergranular fracture and the size of intergranular facets decreased, as evidenced by the observed reduction in intergranular fracture area (Fig. 5). Second, the ferrite-martensite interfaces demonstrate greater resistance to hydrogen embrittlement compared to PAGBs. Because dynamic ferrite transformation basically occurs in accordance with the Kurdjumov–Sachs orientation relationship relative to the parent austenite grain [28], the dynamically transformed ferrite-martensite interface is generally more coherent or semi-coherent and has lower interfacial energy, minimizing the driving force for hydrogen and impurity segregation. In contrast, PAGBs are high-energy, disordered regions that tend to accumulate hydrogen and other impurities, which promote localized decohesion. Moreover, the softer, ductile nature of ferrite mitigates stress concentrations in the harder martensite, dissipating strain energy at the interface and further inhibiting crack initiation even in the presence of hydrogen. Koyama et al. [15] investigated the hydrogen embrittlement behavior in a ferrite/martensite dual-phase steel and revealed that the crack initiated preferentially at PAGBs rather than ferrite-martensite interfaces. The first-principles calculations by Geng et al. [29] suggested that hydrogen leads to more significant decohesion between (110) planes inside the martensite than along the ferrite-martensite interface. This explains why the hydrogen-charged 700HC specimen, which had the highest PAGBs coverage, exhibited only quasi-cleavage fracture. Finally, the distinct differences in carbon content and substructure between ferrite and martensite could significantly affect strain and stress partitioning [34]. These differences influence the crack driving force, hydrogen trapping/subsequent migration during deformation, and the resulting localized effects on decohesion and plasticity [29,35]. Additionally, the ferrite grains can act as barriers to crack propagation, as reported by

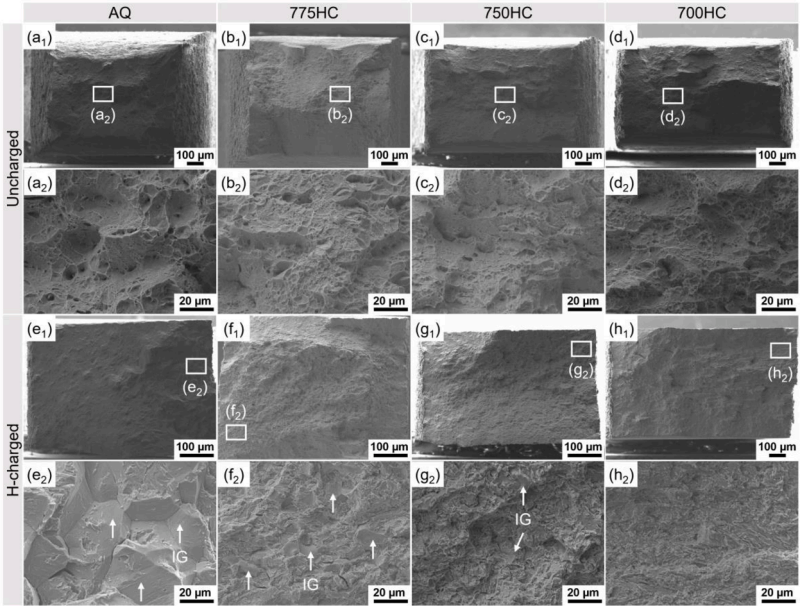

Fig. 5. SEM images of fracture surfaces for (a_1, a_2, e_1, e_2) AQ, (b_1, b_2, f_1, f_2) 775HC, (c_1, c_2, g_1, g_2) 750HC, and (d_1, d_2, h_1, h_2) 700HC specimens, without (a_1–d_1, a_2–d_2) and with (e_1–h_1, e_2–h_2) hydrogen charging. Low-magnification images (a_1–h_1) display the overall fracture morphology; high-magnification images (a_2–h_2), indicated by rectangles in the corresponding low-magnification images, highlight the selected areas. Intergranular (IG) surfaces are marked by white arrows in hydrogen-charged specimens.

Koyama et al. [15]. Further studies will focus on the strain localization, hydrogen distribution (including Kissinger analysis to determine the binding energy of hydrogen traps, secondary ion mass spectrometry, hydrogen microprinting, and three-dimensional atom probe tomography for mapping the spatial distribution of hydrogen), and crack initiation/propagation behaviors to elucidate the detailed mechanisms.

In summary, we developed a novel approach for architecting dual-phase heterostructure consisting of fine martensite substructure and dynamically transformed ferrite grains along the PAGBs to enhance the hydrogen embrittlement resistance in high-strength martensitic steels. This microstructure significantly improved the resistance to hydrogen embrittlement compared to the as-quenched martensite, while maintaining a tensile strength exceeding 1200 MPa. As the deformation temperature decreased, both the ferrite volume fraction and the PAGBs coverage by ferrite increased, which consequently reduced the area fraction of hydrogen-related intergranular fracture. Notably, 60 % compression at 700 °C completely suppressed hydrogen-related intergranular fracture, achieving an exceptional combination of strength and ductility even in hydrogen-charged state. The coverage of PAGBs by dynamically transformed ferrite was a key factor in enhancing the hydrogen embrittlement resistance, with higher coverage correlating with greater hydrogen embrittlement resistance. These findings provide valuable microstructure design concepts for high-strength martensitic steels with superior hydrogen embrittlement resistance. Moreover, the straightforward processing method facilitates industrial implementation by enabling scalable, cost-effective production with minimal disruption to existing manufacturing processes.

CRediT authorship contribution statement

Xiaodong Lan: Writing – original draft, Validation, Methodology, Investigation, Formal analysis, Data curation, Conceptualization. **Kazuho Okada:** Writing – review & editing, Validation, Funding acquisition. **Rintaro Ueji:** Writing – review & editing, Validation, Resources, Methodology. **Akinobu Shibata:** Writing – review & editing, Validation, Supervision, Resources, Project administration, Methodology, Funding acquisition, Conceptualization.

Declaration of competing interest

The authors declare that they have no known competing financial interests or personal relationships that could have appeared to influence the work reported in this paper.

Acknowledgements

This work was financially supported by JSPS KAKENHI (Grant Numbers JP22K18910, JP23H01717, JP23K13541, and JP24K01221) and MEXT Program: Data Creation and Utilization Type Material Research and Development Project Grant Number JPMXP1122684766.

Supplementary materials

Supplementary material associated with this article can be found, in the online version, at doi:10.1016/j.scriptamat.2025.116711.

References

[1] J. Venezuela, Q.L. Liu, M.X. Zhang, Q.J. Zhou, A. Atrens, A review of hydrogen embrittlement of martensitic advanced high-strength steels, Corros. Rev. 34 (3) (2016) 153–186.
[2] I.M. Robertson, P. Sofronis, A. Nagao, M.L. Martin, S. Wang, D.W. Gross, K. E. Nygren, Hydrogen embrittlement understood, Metall. Mater. Trans. A 46 (6) (2015) 2323–2341.
[3] Y. Hagihara, T. Shobu, N. Hisamori, H. Suzuki, K. Takai, K. Hirai, Delayed fracture using CSRT and hydrogen trapping characteristics of V-bearing high-strength steel, ISIJ Int 52 (2) (2012) 298–306.
[4] A. Shibata, T. Murata, H. Takahashi, T. Matsuoka, N. Tsuji, Characterization of hydrogen-related fracture behavior in as-quenched low-carbon martensitic steel and tempered medium-carbon martensitic steel, Metall. Mater. Trans. A 46 (12) (2015) 5685–5696.
[5] S. Morito, H. Tanaka, R. Konishi, T. Furuhara, T. Maki, The morphology and crystallography of lath martensite in Fe-C alloys, Acta Mater 51 (6) (2003) 1789–1799.
[6] S. Morito, X. Huang, T. Furuhara, T. Maki, N. Hansen, The morphology and crystallography of lath martensite in alloy steels, Acta Mater 54 (19) (2006) 5323–5331.
[7] A. Shibata, G. Miyamoto, S. Morito, A. Nakamura, T. Moronaga, H. Kitano, I. Gutierrez-Urrutia, T. Hara, K. Tsuzaki, Substructure and crystallography of lath martensite in as-quenched interstitial-free steel and low-carbon steel, Acta Mater. 246 (2023) 118675. -118675.
[8] M. Wang, E. Akiyama, K. Tsuzaki, Hydrogen degradation of a boron-bearing steel with 1050 and 1300MPa strength levels, Scr. Mater. 52 (5) (2005) 403–408.
[9] A. Shibata, I. Gutierrez-Urrutia, A. Nakamura, K. Okada, G. Miyamoto, Y. Madi, J. Besson, T. Hara, K. Tsuzaki, Three-dimensional propagation behavior of hydrogen-related intergranular cracks in high-strength martensitic steel, Int. J. Hydrogen Energy 48 (88) (2023) 34565–34574.
[10] Y. Momotani, A. Shibata, N. Tsuji, Hydrogen embrittlement behaviors at different deformation temperatures in as-quenched low-carbon martensitic steel, Int. J. Hydrogen Energy 47 (5) (2022) 3131–3140.
[11] C.J. McMahon, Hydrogen-induced intergranular fracture of steels, Eng. Fract. Mech. 68 (6) (2001) 773–788.
[12] Y. Momotani, A. Shibata, D. Terada, N. Tsuji, Effect of strain rate on hydrogen embrittlement in low-carbon martensitic steel, Int. J. Hydrogen Energy 42 (5) (2017) 3371–3379.
[13] Y. Momotani, A. Shibata, T. Yonemura, Y. Bai, N. Tsuji, Effect of initial dislocation density on hydrogen accumulation behavior in martensitic steel, Scr. Mater. 178 (2020) 318–323.
[14] A. Nagao, C.D. Smith, M. Dadfarnia, P. Sofronis, I.M. Robertson, The role of hydrogen in hydrogen embrittlement fracture of lath martensitic steel, Acta Mater 60 (13–14) (2012) 5182–5189.
[15] M. Koyama, C.C. Tasan, E. Akiyama, K. Tsuzaki, D. Raabe, Hydrogen-assisted decohesion and localized plasticity in dual-phase steel, Acta Mater 70 (2014) 174–187.
[16] H.K. Birnbaum, P. Sofronis, Hydrogen-enhanced localized plasticity—A mechanism for hydrogen-related fracture, Mater. Sci. Eng., A 176 (1) (1994) 191–202.
[17] S. Wang, M.L. Martin, P. Sofronis, S. Ohnuki, N. Hashimoto, I.M. Robertson, Hydrogen-induced intergranular failure of iron, Acta Mater 69 (2014) 275–282.
[18] X. Lan, K. Okada, I. Gutierrez-Urrutia, A. Shibata, Quantitative analysis of local plasticity accompanying hydrogen-related fracture in low-carbon martensitic steel, Int. J. Hydrogen Energy 50 (2024) 333–341.
[19] M. Nagumo, K. Takai, The predominant role of strain-induced vacancies in hydrogen embrittlement of steels: overview, Acta Mater 165 (2019) 722–733.
[20] M. Nagumo, T. Yagi, H. Saitoh, Deformation-induced defects controlling fracture toughness of steel revealed by tritium desorption behaviors, Acta Mater 48 (4) (2000) 943–951.
[21] F. Archie, S. Zaefferer, On variant selection at the prior austenite grain boundaries in lath martensite and relevant micro-mechanical implications, Mater. Sci. Eng., A 731 (2018) 539–550.
[22] A. Shibata, I. Gutierrez-Urrutia, A. Nakamura, T. Moronaga, K. Okada, Y. Madi, J. Besson, T. Hara, Local crack arrestability and deformation microstructure evolution of hydrogen-related fracture in martensitic steel, Corros. Sci. 233 (2024) 112092.
[23] A. Shibata, I. Gutierrez-Urrutia, A. Nakamura, G. Miyamoto, Y. Madi, J. Besson, T. Hara, K. Tsuzaki, Multi-scale three-dimensional analysis on local arrestability of intergranular crack in high-strength martensitic steel, Acta Mater 234 (2022) 118053. -118053.
[24] K. Okada, A. Shibata, T. Sasaki, H. Matsumiya, K. Hono, N. Tsuji, Improvement of resistance against hydrogen embrittlement by controlling carbon segregation at prior austenite grain boundary in 3Mn-0.2C martensitic steels, Scr. Mater. 224 (2023) 115043. -115043.
[25] K. Okada, A. Shibata, Y. Kimura, M. Yamaguchi, K.I. Ebihara, N. Tsuji, Effect of carbon segregation at prior austenite grain boundary on hydrogen-related crack propagation behavior in 3Mn-0.2C martensitic steels, Acta Mater 280 (2024) 120288.
[26] M. Pinson, H. Springer, K. Verbeken, T. Depover, The effect of an Al-induced ferritic microfilm on the hydrogen embrittlement mechanism in martensitic steels, Mater. Sci. Eng., A 851 (2022) 143587.
[27] L. Zhao, N. Park, Y. Tian, A. Shibata, N. Tsuji, Combination of dynamic transformation and dynamic recrystallization for realizing ultrafine-grained steels with superior mechanical properties, Sci. Rep. 6 (1) (2016) 39127.
[28] H. Beladi, G.L. Kelly, P.D. Hodgson, Ultrafine grained structure formation in steels using dynamic strain induced transformation processing, Int. Mater. Rev. 52 (1) (2007) 14–28.
[29] W.T. Geng, V. Wang, J.X. Li, N. Ishikawa, H. Kimizuka, K. Tsuzaki, S. Ogata, Hydrogen trapping in carbon supersaturated α iron and its decohesion effect in martensitic steel, Scr. Mater. 149 (2018) 79–83.
[30] F. Hou, Y. Bai, A. Shibata, N. Tsuji, Microstructure evolution during thermomechanical processing in 3Mn-0.1C medium-Mn steel, Mater. Sci. Technol. 35 (17) (2019) 2101–2108.

[31] A. Shibata, Y. Takeda, N. Park, L. Zhao, S. Harjo, T. Kawasaki, W. Gong, N. Tsuji, Nature of dynamic ferrite transformation revealed by in-situ neutron diffraction analysis during thermomechanical processing, Scr. Mater. 165 (2019) 44–49.
[32] H. Kawata, K. Sakamoto, T. Moritani, S. Morito, T. Furuhara, T. Maki, Crystallography of ausformed upper bainite structure in Fe-9Ni-C alloys, Mater. Sci. Eng. A 438 (2006) 140–144.
[33] L.J. Zhao, N. Park, Y.Z. Tian, A. Shibata, N. Tsuji, Deformation-assisted diffusion for the enhanced kinetics of dynamic phase transformation, Mater. Res. Lett. 6 (11) (2018) 641–647.
[34] C.C. Tasan, J.P.M. Hoefnagels, M. Diehl, D. Yan, F. Roters, D. Raabe, Strain localization and damage in dual phase steels investigated by coupled in-situ deformation experiments and crystal plasticity simulations, Int. J. Plast. 63 (2014) 198–210.
[35] A. Turk, G.R. Joshi, M. Gintalas, M. Callisti, P.E.J. Rivera-Díaz-del-Castillo, E. I. Galindo-Nava, Quantification of hydrogen trapping in multiphase steels: part I - Point traps in martensite, Acta Mater. 194 (2020) 118–133.